Thermal Science and Engineering Progress 55 (2024) 102990

Contents lists available at ScienceDirect

Thermal Science and Engineering Progress

journal homepage: www.sciencedirect.com/journal/thermal-science-and-engineering-progress

Design, numerical optimisation and experimental validation of an innovative solar-powered tube heater with multiple air impingement jets

Hadi Tannous [a], Valentina Stojceska [a,b,*], Jose Tavares [b], Savvas Tassou [a,b]

[a] Brunel University London, College of Engineering, Design and Physical Sciences, Uxbridge UB8 3PH, UK

[b] Brunel University London, Institute of Energy Futures, Centre for Sustainable Energy Use in Food Chains, Uxbridge UB8 3PH, UK

ARTICLE INFO

Keywords:
Multiple air impingement jets
Cylindrical target
Steel tube heater
Numerical model
CFD
Experimental validation

ABSTRACT

This research investigates a novel tube heater designed for the seamless integration of an innovative solar thermal system into the powder-based coating process to heat steel tube at a temperature of 240 °C. It incorporates a comprehensive numerical model developed and assessed using ANSYS FLUENT, concentrating on seven critical parameters that significantly influence the tube heater's performance and size. These parameters include tube heater length, jets' length, funnel height, Z/D_{jet}, Y/D_{jet} and X/D_{jet} ratios, as well as jet diameter. The findings underline the critical role of tube heater length in enhancing heat transfer and maximising thermal efficiency, while reducing jet length and funnel height demonstrated negligible effects on thermal performance, promoting material economy. A lower Z/D_{jet} ratio enhanced heat transfer uniformity, improving thermal performance, while optimal X/D_{jet} and Y/D_{jet} ratios were identified as 4, maintaining a balance between heat transfer rate and energy consumption. A smaller jet diameter proved beneficial since the potential core was not achieved, increasing heat transfer to the steel tubes. The experimental model, conducted to validate the novel tube heater's performance, remarkably aligns with the numerical model, showing an R-squared value of 0.992. These results affirm the numerical setup's accuracy and reliability in capturing the tube heater's thermal behaviour. It is concluded that the novel tube heater stands as a highly efficient solution for the seamless integration of solar thermal systems into the powder-based coating process of steel tubes, promising significant emissions reduction.

1. Introduction

Industries are responsible for 37 % of global greenhouse gas (GHG) emissions due to their heavy reliance on fossil fuels to meet their heat and electricity demands [1]. To combat climate change, governments worldwide have set ambitious targets for achieving net-zero emissions by 2050 [2]. This drive towards sustainability has prompted industries to explore renewable energy technologies, with a particular focus on solar thermal energy which is known for its potential to reduce GHG emissions [3].

Currently, there are 635 solar thermal energy collectors in operation worldwide, capable of reaching temperatures up to 400 °C which contribute approximately 441 MWh of heat annually to the industrial processes [4]. However, only 10 % of these collectors are deployed in energy-intensive sectors such as cement, ceramics, chemicals, and iron and steel, while the majority are used in less energy-intensive processes [5]. Notably, the iron and steel industry is one of the largest energy consumers in the EU, with the energy demand exceeding 550 TWh in 2015 [6]. However, it has yet to employ solar thermal energy to its processes operating at the temperature of up to 400 °C [6].

In the iron and steel industry, one of the most energy-intensive processes is the powder-based coating of steel tubes, requiring preheating to a temperature of 240 °C. This process could potentially be powered using solar thermal energy as an alternative to reduce the use of the current method, which employs an electric-based induction heater, thus resulting in significant electricity consumption and high environmental impact [7].

To address these types of industrial issues and reduce GHG emissions, an innovative Solar Heat for Industrial Processes (SHIP) system has been developed. It incorporates a combination of a Fresnel collector and Phase Change Material (PCM) storage for application to industrial processes within the temperature range of 150–400 °C [8,9]. These technologies allows SHIP systems to reduce the use of existing fossil-fuel based systems and subsequently, their emissions. However, the challenge to integrate the SHIP system into the powder-based coating

* Corresponding author at: Brunel University London, College of Engineering, Design and Physical Sciences, Uxbridge UB8 3PH, UK.
E-mail address: Valentina.Stojceska@brunel.ac.uk (V. Stojceska).

https://doi.org/10.1016/j.tsep.2024.102990
Received 29 January 2024; Received in revised form 19 September 2024; Accepted 14 October 2024
Available online 16 October 2024

Nomenclature

$D_{air\text{-}inlet}$	Diameter of the air inlet [mm]
$D_{air\text{-}outlet}$	Diameter of the air outlets [mm]
D_{is}	Diameter of the inner shell [mm]
D_{jet}	Diameter of the jets [mm]
D_{os}	Diameter of the outer shell [mm]
D_{target}	Diameter of the target [mm]
H_{funnel}	Height of the funnel [mm]
L_{jet}	Length of the jets [mm]
L_{os}	Length of the outer shell [mm]
L_{st}	Length of the steel tube [mm]
X/D_{jet}	Ratio of the spacing between jets axially to the jets' diameter
Y/D_{jet}	Ratio of the spacing between jets circumferentially to the jets' diameter
Z/D_{jet}	Ratio of the spacing between the jets and target to the jets' diameter
ρ	Density [kg/m^3]
u	Velocity magnitude [m/s]
t	Time [s]
p	Pressure
μ	Dynamic viscosity [Pa/s]
δ_{ij}	Kronecker delta
μ_t	Turbulent viscosity [kg/m.s]
k	Turbulence kinetic Energy [J/kg]
ω	Specific dissipation rate [s^{-1}]
S	Strain rate magnitude
α^*	Low-Reynolds-number correction coefficient
F_2	Blending function
α	Constant
m	Mass [kg]
c_p	Specific heat [W/kg.K]
dT	Temperature rise [^{o}C]
dP	Pressure difference in between the inlet and outlet of the tube heater [Pa]
dT	Temperature difference in between the inlet and outlet of the tube heater [^{o}C]
P_{fan}	Required fan power [kW]
$\dot{v}_{air}$	Volumetric flow rate of air [m^3/s]
Q	Heat transfer rate [W]
S_x	Error Factor in reading
X	Reading with uncertainty
U_X	Uncertainty of the reading

Abbreviations

ASTEP	Application of Solar Thermal Energy to Processes
CSEF	Centre for Sustainable Energy use in Food chains
EU	European Union
EWT	Enhanced Wall Treatment
GHG	Greenhouse Gasses
PCM	Phase Change Material
SHIP	Solar Heat for Industrial Processes
SST	Shear Stress Transport

process without disruption still remains and is addressed in the present study. A novel tube heater that utilises multiple air impingement jets to transfer the solar heat to the tubes as they move axially is introduced. Jet impingement is a well-established and highly efficient heating technique that has been widely applied to various industries for paper drying, food processing, gas turbine blade cooling, electrical equipment cooling and aircraft blade de-icing [10].

Numerous studies have investigated the thermal performance of jet impingement systems, focusing on optimising critical design parameters such as jet diameter, jet-to-target distance, and spacing between adjacent jets. Some studies focused on single and multiple jet systems with a flat target [10–17], while others considered single and double impingement on a cylindrical target [18–23], depending on their specific application requirements. Looking at the studies that investigated multiple air impingement jet systems, they concentrated on the effect of different critical parameters such as jet-to-jet and jet-to-target spacing, as well as jet shape and inclination angle on the thermal performance.

Some of these studies considered a multiple air jet impingement system with a flat target, such as Chougule et al. [11] who investigated the thermal performance of a 3x3 multiple jet cooling system. The authors developed numerical and experimental models of the system to evaluate both, the most suitable turbulence model and the effect of the distance between the jets and the target (Z/D_{jet}) on the thermal performance. For the turbulence models, they considered the k-ϵ, Renormalisation Group (RNG) k-ϵ, k-ω and Shear Stress Transport (SST) K-ω models, and found that the SST K-ω was the best to predict the flow characteristics in impingement jet systems with a minimal prediction error of 2.1 %. For the Z/D_{jet} ratio, they considered its effect on the Nusselt number, which directly influences the heat transfer rate. Results showed an inversely proportional relationship where increasing the Z/D_{jet} ratio from 6 to 10 led to a decrease in the average Nusselt number from 50.1 to 36.41, subsequently reducing the heat transfer rate. San and Chen [13] developed an experimental model of a five-jet impingement system with a flat target to investigate the effect of jet-to-jet spacing and Z/D_{jet} ratio on heat transfer characteristics. They found that increasing the jet-to-jet spacing from $2D_{jet}$ to $8D_{jet}$ reduced air crossflow, consequently enhancing the heat transfer rate. Conversely, increasing the Z/D_{jet} ratio from 0.5 to 3 increased air crossflow, reducing the heat transfer rate. Yong et al. [23] experimentally investigated the effect of jet-to-target spacing, jet-to-jet spacing and jets' alignments on the heat transfer in a multiple-air jet impingement system with a flat target. The authors considered jet-to-target spacing between $2D_{jet}$ and $4D_{jet}$, jet-to-jet spacings between $2D_{jet}$ and $5D_{jet}$, and two jet alignments: inline and staggered. Results showed that decreasing jet-to-target spacing increased the heat transfer rate, observing optimum values of $2D_{jet}$. Similarly, decreasing the jet-to-jet spacing also decreased the heat transfer rate, but the optimum value was found at $3D_{jet}$, as at a lower value of $2D_{jet}$, air crossflow and jet interaction increased, reducing the heat transfer rate. Finally, inline alignment achieved the best heat transfer at $3D_{jet}$, while staggered alignment was more efficient at $5D_{jet}$. Rao et at. [10,17] developed a multiple impingement system with micro jets for cooling flat equipment. The authors designed a geometry with a funnel-shaped inlet that distributed the air equally to each of the jets in flat impingement plate. They investigated the effect of jets diameter on the heat transfer rate and found that decreasing its value at a constant jet-to-jet spacing will lead to a higher heat transfer rate due to the increase in the overall number of jets in the system. The authors also investigated the effect of having one of the micro jets clogged and found this to lead to a decrease in the heat transfer rate by 6 % and an increase in the pressure drop by 15 %.

Other studies considered a multiple air impingement jet system with a cylindrical target, such as Csernyie and Straatman [19] who conducted a computational study on an impingement system for a cylindrical target with axially aligned jets. Their parametric analysis evaluated the effects of Z/D_{jet} ratio, the axial jet-to-jet spacing (X/D_{jet}), and the ratio of the jets' diameter to the target's diameter (D_{jet}/D_{target}) on the Nusselt number and heat transfer rate. Results showed that decreasing the Z/D_{jet} ratio from 2.1 to 0.2 and increasing the D_{jet}/D_{target} from 0.15 to 0.31 will lead to a higher Nusselt number and consequently, a higher heat transfer rate. No clear trend was observed in the Nusselt number when varying the X/D_{jet} ratio where a constant value was obtained for X/D_{jet} greater than 2.9 due to low jet interference. Jordan et al. [24] investigated the effect of the shape of axially aligned jets on the heat transfer in their impingement system. They considered cylindrical and racetrack-shaped jets with square-edged, partially filleted, and fully filleted inlets and outlets. Results showed the racetrack-shaped jets provided enhanced heat transfer compared to the cylindrical ones, whereas increasing the degree of filleting of the inlets and outlets decreased the heat transfer rate. Shi et al. [25] experimentally investigated heat transfer characteristics of different inclination angles of circumferentially arranged jets in their impingement cooling system. The authors considered Reynolds numbers between 20,000 and 35,000 and jet inclination angles of 20°, 30° and 45°. They concluded that increasing the Reynolds number to 35,000 led to an increase of 64.3 %-74.9 % in the Nusselt number, enhancing the heat transfer, whereas increasing the incident angle to 45° reduced the uniformity of the heat transfer.

None of these studies considered a cylindrical distribution of the jets but were limited to either an axial or a circumferential alignment. According to the authors' best knowledge, no previous study has explored the thermal performances of multiple air impingement systems with a cylindrical distribution of the jets for cylindrical targets that can be adapted to the solar-powered tube heater.

Therefore, this paper aims to develop a novel tube heater that transfers solar heat from the SHIP system to the steel tube in the powder-based coating process using multiple air impingement jets. This is achieved in two stages: Firstly, a numerical model of the tube heater is developed to analyse its thermal performance and carry out a parametric analysis of seven critical parameters to optimise its design. Secondly, an experimental model is developed to replicate the numerical model in a practical laboratory environment and validate its results. The parameters investigated in the parametric analysis include parameters like the spacing between the jets and the target, the axial and circumferential spacing between the jets and the jet's diameter, which have been considered in previous studies on impingement systems. It also includes additional parameters that are critical to the overall design of the tube heater, namely, its length and height, and the jet's length. Parameters such as the shape of the jet and its inclination angle were not considered in this study due to manufacturing and financial limitations.

2. Methodology

The methodology involves two parts: development of a new numerical model of the novel tube heater (2.1) and its experimental validation (2.2).

2.1. Numerical model

The numerical model of the novel tube heater focuses on assessing and optimising its thermal performance through a comprehensive parametric analysis. It included 34 simulations that examine the effect of seven critical parameters on the thermal performance, as follows: Firstly, the conceptual design of the tube heater and 3D geometries are developed using SolidWorks (Massachusetts Institute of Technology, USA), as presented in 2.1.1. Secondly, the meshes of the geometries are generated and analysed, as presented in 2.2.2. Thirdly, the solution is set up using ANSYS FLUENT (ANSYS, Inc., USA) and presented in 2.1.3. Finally, the aspects considered for the results analysis to obtain the optimum design of the tube heater are presented in 2.1.4.

2.1.1. Design the tube heater

The design of the tube heater is carefully tailored to meet the specific requirements of the steel tube powder-based coating process. The conceptual design of the tube heater is presented in Fig. 1 and its 3D geometry in Fig. 2. The multiple jet impingement system considered in this study was adapted from Rao et al. [10,17] who previously applied it for cooling of micro turbines and electronic chips. They used a flat jets' impingement plate to meet the shape of their target. For this study, the jet's impingement plate was amended into a jet impingement cylinder to suit the shape of the tubes. [10,17]Hence, the tube heater was designed to incorporates two major parts, the inner and the outer shells. The inner shell includes the impingement jets cylinder and two air outlets with a primary function to impinge high-velocity air uniformly onto the steel tube from all directions. The outer shell serves as the boundary for the airflow and incorporates a funnel-shaped inlet. Notably, it was important to achieve equal air distribution to all the jets to ensure uniform heating of the tube from all directions. For this reason, the inlet was placed at the centre top of the system, whereas the outlets were placed on each end of bottom side. In addition, the cross-sectional areas of both were kept equal, preventing excessive pressure drop. This lead the hot air supplied by the SHIP system to enter into the tube heater from the top, flows through the impingement jets heating the tubes from all directions then exits from the bottom through the two air outlets.

In order to improve the design, the critical parameters in the inner and outer shells (Fig. 2), were optimised. These include seven parameters: (i) the height of the funnel (H_{Funnel}), (ii) the length of the outer shell (L_{OS}), (iii) the jets' length (L_{jet}) which depends on the shell's thickness, (iv) the distance between the jets and the tube (Z/D_{jet}), (v) the axial (X/D_{jet}) and (vi) circumferential (Y/D_{jet}) spacing between the jet; and (vii) the jets' diameter (D_{jet}) (Fig. 2).

A total of 34 geometries were developed in SolidWorks for the parametric analysis of the tube heater. These considered different values for the seven critical parameters (Fig. 2) to analyse each individually.

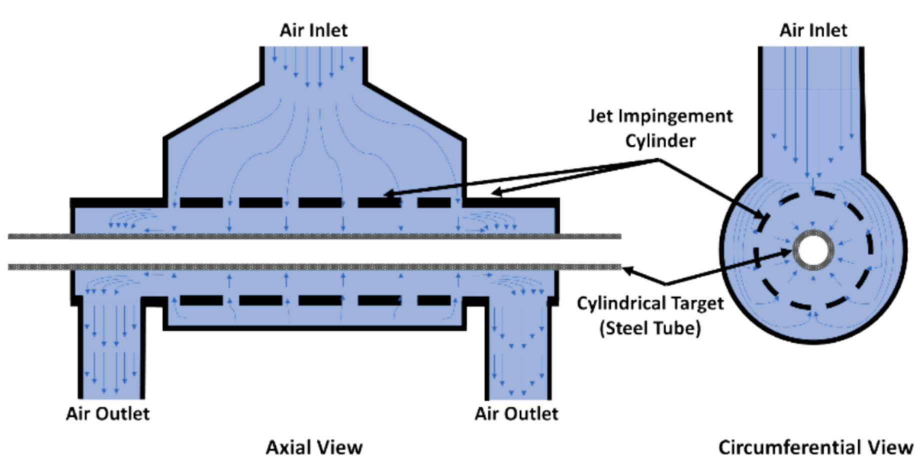

Fig. 1. Conceptual design of the novel tube heater.

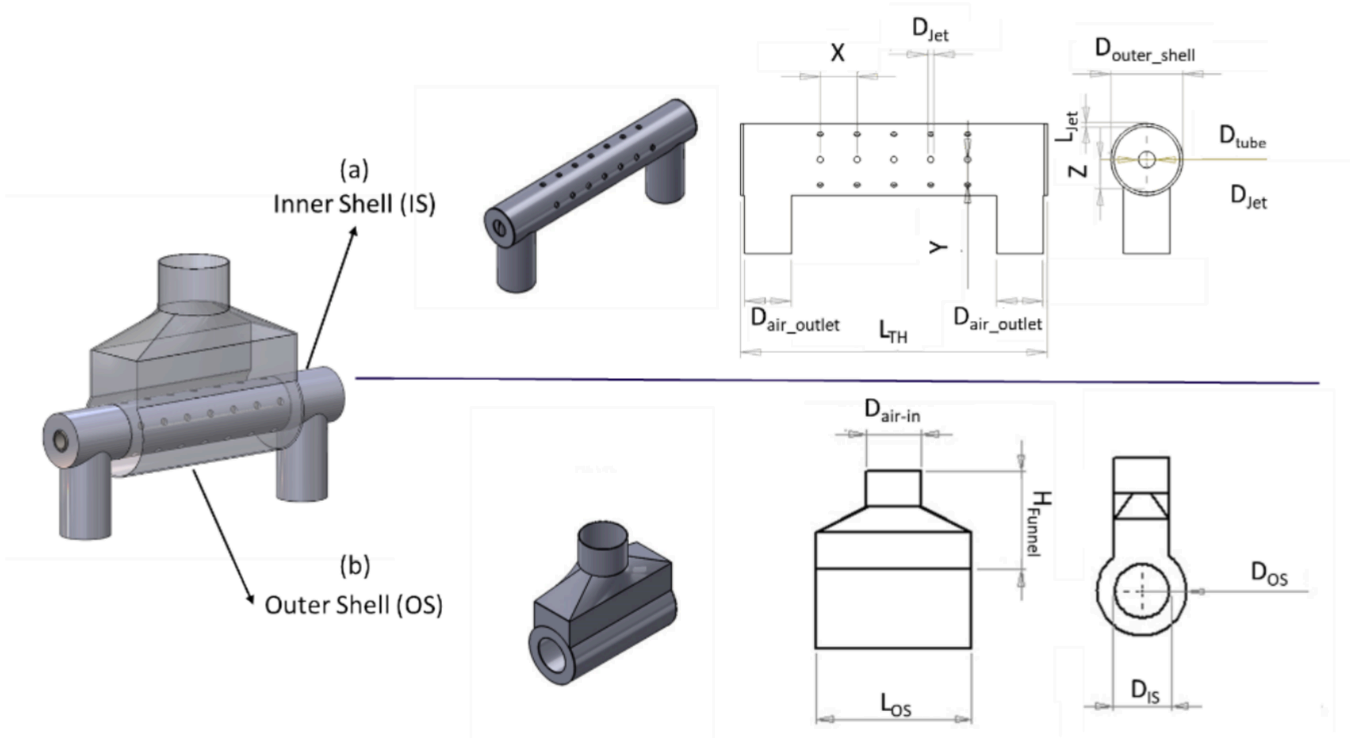

Fig. 2. Critical parameters of the (a) outer and (b) inner shell of the tube heater.

They are imported to the ANSYS Design Modeller where the *Steel Tube* and *Airflow* parts are obtained and combined into a single entity to prevent the geometry of being meshed into disconnected bodies [26].

2.1.2. *Meshing*

The meshing of the geometries involved selecting tetrahedral meshing for the *Airflow* part and hexahedral meshing for the *Steel Tube* part. Additionally, *face sizing* and inflation of five layers were applied at the steel tube's wall where the generation of the mesh was set to start. This smoothened the mesh generation achieving a high-quality mesh, and consequently, accurate results. The *face sizing* functions was also applied to enhance the meshes' quality. Fig. 3 presents the mesh of the *Airflow* part (Fig. 3a), the *Steel tube* part (Fig. 3b) and alignment between them (Fig. 3c) since they have been specified as a single entity in ANSYS Design Modeller (Section 2.1.1). The mesh achieved an average and maximum skewness of 0.24 and 0.68, respectively, along with an orthogonal quality of 0.29, which is considered as a good/acceptable mesh quality [27].

A grid independence test was conducted to determine the optimal number of elements for the mesh with minimal computational cost and time. Table 1 compares four different meshes of the preliminary design (Fig. 1) with varying numbers of elements in terms of the results

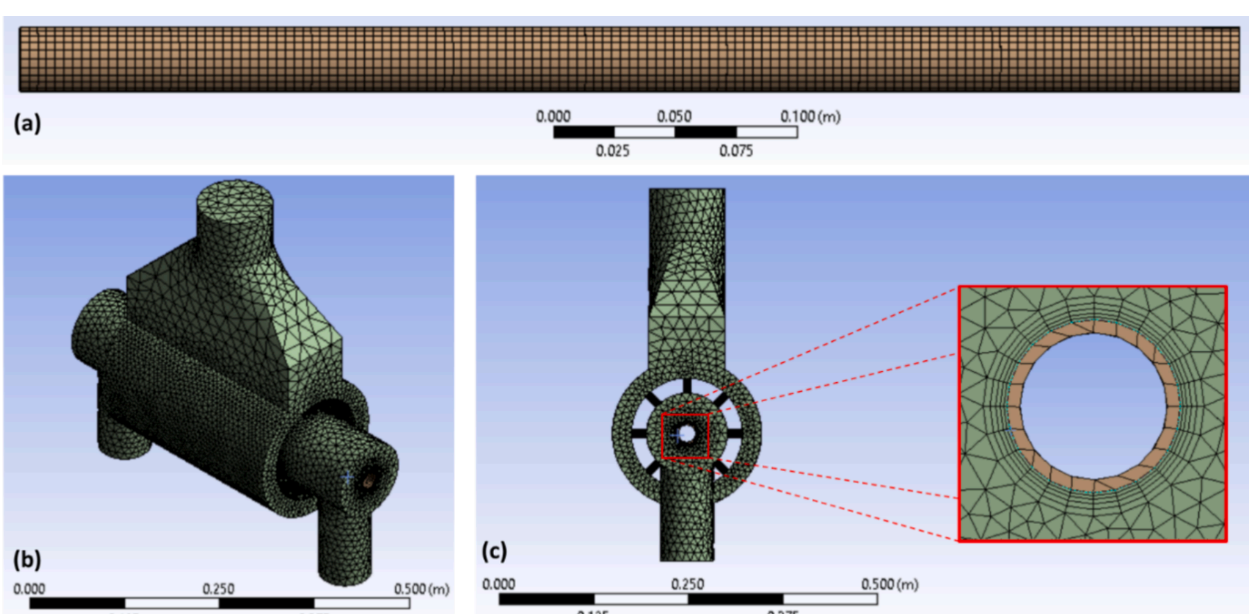

Fig. 3. Meshing of the tube heater Steel Tube (a), airflow region (b) and the mesh alinement between them (c).

Table 1
Grid independence test.

	Mesh 1	Mesh 2	Mesh 3	Mesh 4
Element size [m]	**0.025**	**0.005**	**0.0035**	**0.0025**
Number of Elements	**775,421**	**1,067,772**	**1,629,321**	**3,186,892**
Heat Transfer Rate [W]	1599	1607	1601	1641
Difference compared to the finest mesh (Mesh 4) [%]	2.6	2.6	2.4	n/a
Pressure drop [Pa]	6717	6848	6838	6802
Difference compared to the finest mesh (Mesh 4) [%]	1.2	0.8	0.5	n/a
Stagnation Velocity [m/s]	104.3	104.7	105	104.6
Difference compared to the finest mesh (Mesh 4) [%]	0.3	0.1	0.4	n/a

obtained for the pressure drop, stagnation velocity and heat transfer rate in the tube heater. The results show that reducing the number of elements in the finest mesh (Mesh 4) from 3,186,892 to 1,629,321 (Mesh 3) 1,067,772 (Mesh 2) and 775,421 (Mesh 1) led to a difference in the results of up to 2.4 %, 2.6 % and 2.6 % respectively. Considering the similarity in the results of the tests, Mesh 1 with the minimum number of elements was selected as the optimal mesh.

2.1.3. Solution set-up

The solution was set up using ANSYS FLUENT to analyse the thermal performance of the tube heater as follows: Firstly, the turbulence was described using the SST K-ω model which strikes a balance between computational cost and accuracy when compared to experimental tests in jet impingement systems [11,18,28]. This model employs the Reynolds averaged Navier-Stokes (RANS) equations (Equations (1) and (2) as the transport equations for the mean flow quantity where ρ is the density, u is the velocity magnitude, t is time, p is pressure, μ is the dynamic viscosity δ_{ij} is the Kronecker delta and $\rho\overline{u_i'u_j'}$ is the Reynolds stress. To close the equations, the Reynolds stresses based on the turbulent viscosity (μ_t) in Equations (3) and (4) where k is the turbulence kinetic energy, ω is the specific dissipation rate, S is the strain rate magnitude, α^* is a coefficient to damp the turbulent viscosity causing a low-Reynolds-number correction, F_2 is the blending function and α_1 is a constant [27,28]. Notably, the SST k-ω model uses the enhanced wall treatment (EWT) which is y + insensitive. In other words, although it may overpredict turbulence levels in large normal strain, it allows a smooth transition from a viscous sub-layer to a wall function. The integration of ω all the way to the wall eliminates the need for damping functions and high-resolution mesh in the near-wall region, features typically required in Low-Reynolds models [29]. Secondly, the material of the *Airflow* and *steel tube* parts were selected as "Air" and "Stainless Steel 235j," respectively, in accordance with data provided for the innovative SHIP system [30]. Notably, no specific material is selected for the outer and inner shells, since they are considered walls during the identification of boundary conditions, a measure taken to reduce computational cost and time. Thirdly, the boundary conditions included specifying the walls as adiabatic and set to no-slip condition, as well as setting the air inlet flow rate to 0.28 kg/s and temperature of 240 °C, in accordance with data provided for the innovative SHIP system [11,15,24]. Fourthly, the solution setup for the model included selecting the pressure–velocity coupling method as "coupled" with second order upwind spatial discretisation to achieve higher accuracy in capturing gradients and flow details. The energy equation was also discretised using the second order upwind scheme to accurately resolve temperature gradients. The residual convergence criteria were set to 10^{-6} for all equations (continuity, momentum, energy, and turbulence), ensuring that the solution reached a high level of accuracy. These stringent solution controls were chosen to provide a robust and accurate simulation framework, ensuring high quality of the numerical results.. Additionally, a temperature gradient contour was generated over the tube wall, and the minimum, average, and maximum temperatures were recorded throughout the simulation. Finally, the simulation was initialised and run using 40 processors in parallel, running for 20 timesteps with a time step size of 0.5 s and 50 iterations per timestep. The time step size was obtained based on the time step independent analysis carried out in Table 4. A suitable timestep size is that with a Courant number (CFL) less than or equal to 1. In the case of the current model, this is equivalent to a timestep size of 0.001 s. It was extremely computationally expensive to observe a significant heat transfer with such a small time step size and comparing to the experimental results. Hence, higher sizes where considered and an optimum value of 0.5 s was obtained (Table 2) where it minimises the computational time without significantly effecting the results.

$$\frac{\partial \rho}{\partial t}+\frac{\partial}{\partial x_i}(\rho u_i)=0 \tag{1}$$

$$\frac{\partial}{\partial t}(\rho u_i)+\frac{\partial}{\partial x_j}(\rho u_i u_j) = -\frac{\partial p}{\partial x_i}+\frac{\partial p}{\partial x_j}\left[\mu\left(\frac{\partial u_i}{\partial x_j}+\frac{\partial u_j}{\partial x_i}-\frac{2}{3}\delta_{ij}\frac{\partial u_l}{\partial x_l}\right)\right]+\frac{\partial}{\partial x_j}\left(-\rho\overline{u_i'u_j'}\right) \tag{2}$$

$$-\rho\overline{u_i'u_j'}=\mu_t\left(\frac{\partial u_i}{\partial x_j}+\frac{\partial u_j}{\partial x_i}\right)-\frac{2}{3}\left(\rho k+\mu_t\frac{\partial u_k}{\partial x_k}\right)\delta_{ij} \tag{3}$$

$$\mu_t=\frac{\rho k}{\omega}\frac{1}{\max\left[\frac{1}{\alpha^*},\frac{SF_2}{\alpha_1\omega}\right]} \tag{4}$$

2.1.4. Results analysis

The next step is to conduct parametric analysis to assess each critical parameter in two main aspects: (i) its influence on the thermal performance of the tube heater and (ii) its impact on the size of the tube heater. Firstly, the change in stagnation velocity at the jets, the heat transfer rate to the steel tube and the pressure drop in the system obtained from ANSYS FLUENT were analysed to evaluate the influence of each parameter on the thermal performance. The stagnation velocity is obtained from the velocity contour of the airflow in the tube heater by measuring the maximum value near the stagnation point, where the air hits the target and loses its axial velocity, causing the static pressure to suddenly rise [12]. The pressure drop is calculated based on the difference between the total pressure at the inlet and the two outlets (Fig. 2). The heat transfer rate is obtained from the flux report in FLUENT which is calculated based on the mass (m), specific heat (c_p) and the temperature rise (dT) of the steel tube following Equation (5) [27].It is crucial to achieve a higher heat transfer rate with minimal pressure drop to avoid high required fan power to run the SHIP system and increase energy savings. Hence, when analysing the results of the parametric analysis the heat transfer rate is compared to the required fan power, as calculated in Equation (7), conjugating the pressure drop (dP) and the volumetric flow rate of air inlet ($\dot{v}_{air}$). Secondly, the change in the size of the tube heater when varying each parameter is analysed to reduce material resources and cost while not significantly compromising the system's thermal performance.

Table 2
Time step size independent analysis.

Timestep size [s]	**0..001**	**0.01**	**0.1**	**0.5**
Heat Transfer Rate [W]	1599	1607	1601	1641
Difference compared to the smallest time step size (0.5 s) [%]	2.6	2.6	2.4	n/a
Pressure drop [Pa]	6717	6848	6838	6802
Difference compared to the smallest time step size (0.5 s) [%]	1.2	0.8	0.5	n/a
Stagnation Velocity [m/s]	104.3	104.7	105	104.6
Difference compared to the smallest time step size (0.5 s) [%]	0.3	0.1	0.4	n/a

$$Q = m \bullet c_p.dT \tag{5}$$

$$P_{fan} = dP \bullet \dot{v}_{air} \tag{6}$$

2.2. Experimental validation

The experimental model of the newly developed tube heater involves assessing its thermal performance to validate the numerical model. The validation process comprises of three stages: (i) setting-up a test rig designed to evaluate the thermal performance of the tube heater (2.2.1); (ii) conducting experimental test to validate the numerical model (2.2.2); (iii) performing an uncertainty analysis of the experimental tests to evaluate potential sources of error and their impact on the results (2.2.3).

2.2.1. Setting-up of the new test rig

Fig. 4 presents a schematic of the test rig which was set up to include the novel tube heater with extended inlet, a hot air loop, high temperature hoses, a Y-piece, a steel tube with attached thermocouples and a data logger. The hot air loop contains an electric duct air-heater and a fan to produce hot air at the required flow rate and temperature. The tube heater was manufactured by the fluid handling systems specialist Orbital Fabrication Ltd. (Cambridge, UK) based on the optimum design obtained from the parametric analysis (Section 2.1.4). It was connected to a hot air loop using high-temperature hoses and the Y-piece which are well insulated using 50 mm double-sided grey silicone jackets with -aerogel infills to reduce thermal losses. Furthermore, a $15D_{air\text{-}inlet}$ extended inlet of the tube heater was installed to ensure fully developed flow. It was monitored using pitot tube and nine thermocouples were strategically installed at critical locations including the air inlet, two outlets and around the tube to capture the temperature distribution in the system. Finally, a steel tube is placed in the tube heater and six thermocouples were soldered to its surface to monitor the tube's temperature rise and report to the data logger.

It's important to acknowledge that the current air loop has operational limitations, preventing it from providing hot air to the tube heater at a temperature of 240 °C and a flow rate of 0.28 kg/s, as simulated in the numerical models (Section 2.1.3). These limitations are associated with the operational speed of the fan and the temperature tolerance of the valves used in the air loop. Hence, the numerical model was validated based on the maximum inlet temperature and flow rate achieved by the air loop. The temperature was measured using a thermocouple at the inlet of the tube heater. Concurrently, the velocity was measured using a pitot tube which was installed in the extended inlet of the tube heater. Both the thermocouples and the pitot tube where calibrated to ensure high accuracy of the results. The thermocouples were carefully calibrated using both an ice bath and a hot-water bath, while the pitot tube was calibrated by a professional third-party calibration service.

2.2.2. Experimental tests setup

The testing of the tube heater involved the following key steps: (i) Activation of the hot air loop to its maximum temperature and airflow settings until it reached steady state. The inlet air temperature stabilised at 150 °C as confirmed using the air thermocouple at the tube heater's inlet. Simultaneously, the pitot tube placed at the extended inlet measured the achieved airflow velocity, capturing both horizontal and vertical distribution. It revealed a developed velocity profile with an average of 12.45 m/s. (ii) Following the stabilisation of the inlet airflow, a steel tube with dimensions similar to those in the numerical model was placed in a steady condition inside the tube heater with the help of the rollers (Fig. 4). Six thermocouples were soldered at various locations on the tube's surface, distributed both circumferentially and longitudinally along the tube to monitor temperature uniformity. (iii) The steel tube remained within the tube heater for 360 s, recording its temperature rise

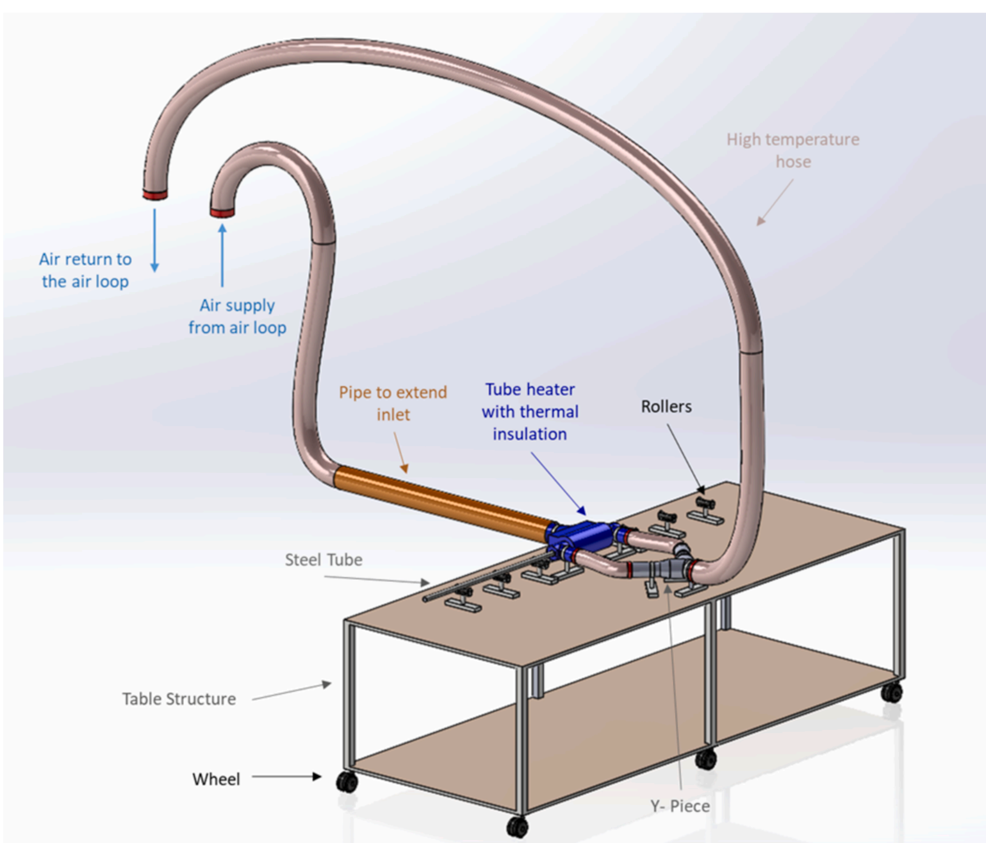

Fig. 4. Schematic of the newly built test rig.

every second through a data logger. (iv) To ensure accuracy, the test was conducted three times, and the experimental results were averaged to determine the temperature rise of the steel tube. (v) A numerical model was developed with the same air inlet temperature and velocity conditions as the experimental test. (vi) The experimental and numerical results were compared using the R-squared method and the error plot. The R-squared method quantified the agreement between the two datasets using Microsoft Excel's built-in function. Additionally, the error plot illustrated the percentage error between the numerical and experimental results, revealing the alignment between the two sets of data.

2.2.3. Uncertainty analysis

In the context of ensuring the reliability of the experimental results, an uncertainty analysis was conducted to assess the potential impact of equipment uncertainties, such as thermocouples and the pitot tube, on the results. The method followed is similar to Baydar and Ozmen [31] who analysed individual uncertainties in their experiment model of an air impingement system with a flat target. The authors identified uncertainty in equipment used to obtain axial velocity, turbulence viscosity, and static pressure measurements, obtaining an uncertainty between 1 % and 6 %. In this study, the uncertainties are associated with the thermocouples used to measure the temperatures of the steel tube and air, as well as pitot tube used to measure the air velocity. Each source of uncertainty is quantitatively analysed using Equation (7) which calculates the uncertainty of each reading, U_x, based on the error factor of the equipment used, S_x, and the reading obtained, X. This well-established analytical approach is employed, as outlined by Tylor [32] and utilised in previous studies such as Mroue et al. [33] for their experimental investigations. This analysis was applied to the readings of the thermocouples used to measure the temperature of the air and the steel tube, recognised for an error factor of $\pm$ 2.5 °C [34] and the pitot tube, characterised by an error factor of $\pm$ 1.5 %. It is important to note that uncertainty below 10 % suggest a negligible impact on the accuracy of the experimental data [32].

$$U_X = \frac{S_X}{X} \tag{7}$$

3. Results and discussion

3.1. Numerical results

This section presents and discusses the outcomes of the parametric analysis to determine the optimal values for the critical parameters that include the tube heater length, jet length, funnel height, Z/D_{jet}, Y/D_{jet}, and X/D_{jet} ratios, as well as jets' diameter.

3.1.1. Tube heater length

The length of the tube heater plays a crucial role in determining both its size and the heat transfer rate to the steel tube. Optimising this parameter is essential to enhance the thermal performance of the system. Table 2 provides an overview of five tests conducted to analyse different tube heater lengths. It is evident that altering the tube heater's length directly impacts the lengths of the outer (L_{OS}) and inner (L_{IS}) shells, as well as the steel tube (L_{st}). Additionally, the ratio of the funnel's inlet (round) to outlet (rectangle) area decreases as the tube heater size decreases. Similarly, the number of axial jets decreases with decreasing tube heater length, except for Tests 1 and 2, where a similar number of jets fit along the inner shell.

The results of Tests 1 to 5, including the pressure drop between the air inlet and outlet, the maximum air velocity obtained at the stagnation point, and the heat transfer rate from the air to the steel tube are presented in Table 2. It is observed that as the tube heater's length degreases, the pressure drop and stagnation velocity increase, resulting in higher average tube temperatures. This trend arises from two main reasons, firstly, the decrease in the volume of the tube heater as its length decrease, and secondly, the decrease in the number of jets as the tube heater's length decreases (Table 2).

While higher pressure drops and velocities theoretically lead to greater heat transfer rates, this relationship did not hold true in Tests 1 to 5. This is because the size of the steel tube absorbing the heat also decreases proportionally, resulting in a proportional decrease in the heat transfer rate. Consequently, it can be concluded that a longer tube heater leads to a higher heat transfer rate. Given the limited available space at the case study, the optimal tube heater length is selected as 500 mm (Test 1).

3.1.2. Jets length

The length of the jets, represented as the thickness of the inner shell, significantly influences the material usage within the system. Optimising this parameter to minimise its value can result in substantial material savings without substantially affecting the system's thermal performance. To the author's best knowledge, no prior studies have investigated the importance of jet length in impingement heating systems. Therefore, Table 3 provides a comparison between Test 1 and Tests 6 and 7, featuring geometries with reduced jet lengths of 10 mm and 5 mm, respectively. These tests aim to evaluate the potential material savings achievable by decreasing jet thickness without compromising the heater's thermal performance.

Table 3 summarises the results of the jets length analysis carried out in Tests 1, 6, and 7. It is evident that reducing the jets length leads to a slight increase in pressure drop and velocity. as anticipated. Consequently, Test 6 exhibits a slight improvement in heat transfer rate, while Test 7 experiences a slight decrease. To further understand this trend, velocity profiles for these tests were generated and are presented in Fig. 5. It can be seen that in all three tests show, the impinged air in the central jets follows a linear path perpendicular to the target, whereas it deviates towards the jet exits in the side jets. This deviation is attributed to air crossflow from the central jets, a phenomenon common in multiple jet impingement systems [10,13]. Notably, this effect becomes more pronounced as jets length decreases (Fig. 5), leading to decreased heat transfer in Test 7. However, the impact of air crossflow on heat transfer rate can be reduced by adjusting the X/D_{jet}, Y/D_{jet}, and Z/D_{jet} ratios [10,13]. Hence, the optimum height is chosen based on its effect on the tube heater's size and cost. Reducing jet length from 10 mm (Test 6) to 5 mm (Test 7) results in a reduction of inner shell size by over 50 %, significantly impacting material usage and system cost. Therefore, the optimal jet length for the tube heater is determined to be 5 mm (Test 7).

3.1.3. Funnel height

The funnel component represents one of the largest and most expensive parts of the tube heater, primarily due to its complex round-to-rectangle design. Optimising this parameter aims to minimise material usage without compromising the system's thermal performance. Several studies have previously incorporated funnel-shaped inlets for multiple jet impingement systems [10,17,35]. However, none have explored the optimal dimensions for this critical component. Consequently, Table 4 offers a comparison between Test 7 and Tests 8, 9, and

Table 3
Tube heater's length analysis.

	Test 1	Test 2	Test 3	Test 4	Test 5
Outer Shell Length [mm]	500	450	300	350	300
Inner Shell Length [mm]	500	450	300	350	300
Steel Tube Length [mm]	300	250	200	150	100
Funnel Area Ratio	3.82	3.18	2.55	1.91	1.27
No. of Jets – axially	5	5	4	3	2
No. of Jet – Circumferential	8	8	8	8	8
Total Number of Jets	40	40	32	24	16
Pressure drop [Pa]	**12,056**	**12,070**	**17,634**	**31,153**	**68,411**
Stagnation velocity [m/s]	**179**	**181**	**225**	**274**	**407**
Heat Transfer Rate [W]	**1733**	**1638**	**1495**	**1453**	**1273**

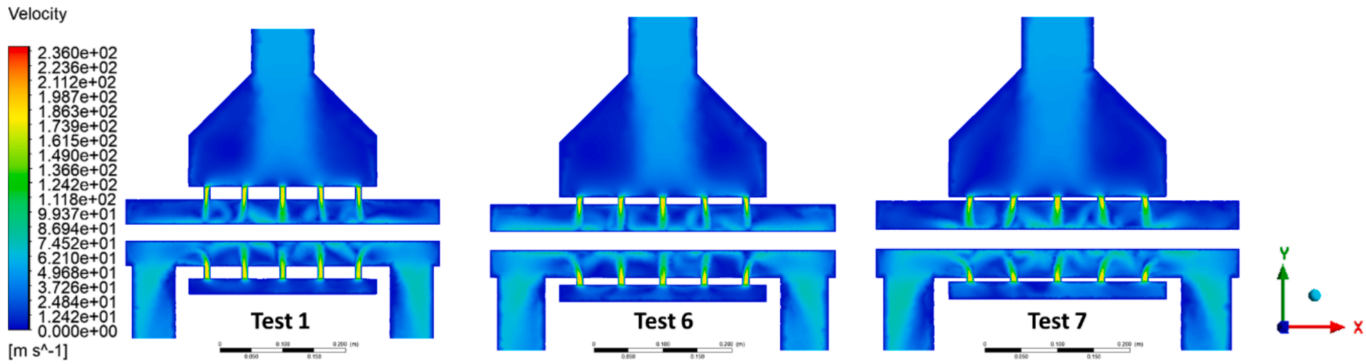

Fig. 5. Velocity profile for tube heater with varying jet length.

Table 4
Jet length analysis.

	Test 1	Test 6	Test 7
Jets length [mm]	20	10	5
Inner Shell thickness [mm]	20	10	5
Outer Shell Diameter [mm]	196.9	176.9	166.9
Pressure drop [Pa]	**12,056**	**13,182**	**14,110**
Stagnation velocity [m/s]	**179**	**186**	**189**
Heat Transfer Rate [W]	**1733**	**1757**	**1757**

10, each featuring different funnel heights corresponding to various round-to-rectangle height configurations of 50, 150, and 200 mm, respectively. These tests are conducted to evaluate the potential material savings while maintaining thermal performance.

Table 4 displays the outcomes of the funnel height analysis conducted in Tests 7, 8, 9, and 10. The results indicate that altering the height of the funnel has minimal impact on pressure drop, stagnation velocity, and heat transfer rate. While it might have been expected that increasing the funnel height would result in more uniform air distribution along the axial length of the tube heater, its effect appears negligible when compared to the air crossflow phenomenon observed in multiple jet impingement systems. This crossflow phenomenon tends to increase pressure drop in the side jets [10], ultimately contributing to a more uniform air distribution in the outer shell (Fig. 6). Consequently, when considering the potential material savings and the negligible difference in heat transfer rate, which can be further optimised by adjusting Z/D_{jet}, Y/D_{jet}, and Z/D_{jet} values [10,13], the optimal round-to-rectangle height was determined to be 50 mm (Test 8).

3.1.4. Spacing between the jets and the target (Z/D_{jet})

The Z/D_{jet} ratio significantly influences the velocity profile of impinged air and its heat transfer rate to the steel tube. Optimising this parameter is crucial to minimise material usage while maintaining thermal performance. Several studies have investigated the impact of the Z/D_{jet} ratio on heat transfer in jet impingement on a cylindrical target. For instance, Tawfek [21] conducted experimental work on circular jet impingement on a cylindrical target, varying the Z/D_{jet} ratio from 7 to 30 for Reynolds numbers ranging from 3,800 to 40,000. The findings indicated that as the Z/D_{jet} ratio increased, the heat transfer rate decreased. Similar conclusions were drawn in subsequent studies examining heat transfer in single [18] and twin [22] jet impingement on a cylindrical target. These studies investigated Z/D_{jet} values ranging from 4 to 16 and observed a decrease in heat transfer rate as Z/D_{jet} increased [18], with the effect being significant only when Z was less than the target's diameter [22]. A similar conclusion was observed by other studies. Chougule et al. [11] investigated of heat transfer characteristics of multiple air jets impingement on a flat plate. At a Reynolds number of 11,000, the authors found the Nusselt number to decrease from 50.1 to 36.41 as Z/D_{jet} increased from 6 to 10, subsequently affecting the heat transfer rate. San and Chen [13] evaluated the effect of Z/D_{jet} on the thermal performance of their multiple jets impingement system with a flat target, and found that increasing Z/D_{jet} ratio from 0.5 to 3 will lead to lower heat transfer rate. Csernyie and Straatman [19] evaluated the effect on a system with a cylindrical target and found that higher values in the rage of 0.2–2.1 will lead to lower Nusselt number and heat transfer rate.

Taking these findings into account, Table 5 compares Test 8 with Tests 11 and 12, which have a Z/D_{jet} ratio of 3 and 2, respectively. The Z/D_{jet} ratio influences the diameters of the inner and outer shells. Therefore, at a constant Y/D_{jet} ratio, a decrease in the number of jets circumferentially occurs, resulting in higher pressure drop, velocity, and heat transfer rate. To isolate the effect of varying the Z/D_{jet} ratio on heat transfer, Tests 13 and 14 with the same number of jets (eliminating the

Table 5
Funnel height analysis.

	Test 8	Test 7	Test 9	Test 10
Funnel height [mm]	190	240	290	340
Round to rectangle height [mm]	50	100	150	200
Pressure drop [Pa]	**14,087**	**14,110**	**13,676**	**13,222**
Stagnation velocity [m/s]	**191**	**189**	**191**	**189**
Heat transfer rate [W]	**1748**	**1757**	**1697**	**1795**

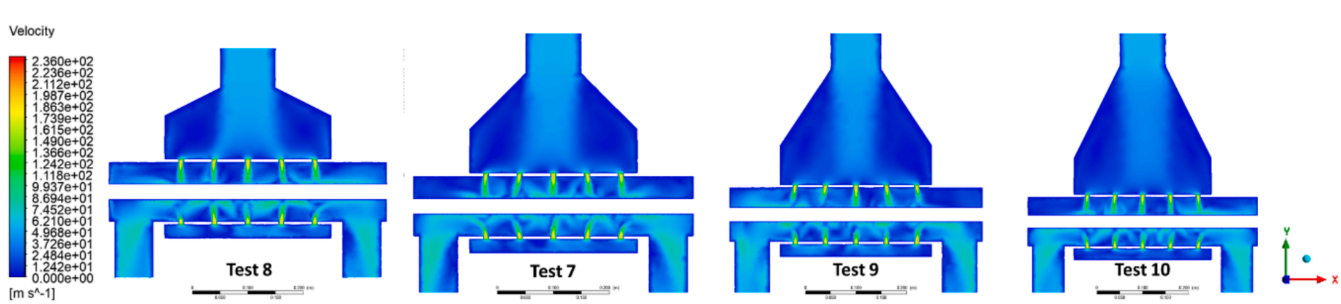

Fig. 6. Velocity profile for tube heater with varying funnel height.

influence of changing the Y/D_{jet} ratio) were compared to Test 8.

The results show that as the Z/D_{jet} ratio decreases in Tests 11 and 12, pressure drop, stagnation velocity (Table 5), and heat transfer rate increase, aligning with the results reported in the literature [11,13,18,21,22]. Furthermore, the results of Tests 13 and 14 show a lesser increase compared to Tests 11 and 12. This suggests that reducing the Z/D_{jet} value enhances the thermal performance of the system, irrespective of the Y/D_{jet} ratio change.

Considering the axial movement of the tube, it is essential to achieve uniform circumferential heat transfer. This is evident in the temperature contour of the steel tube, as shown in Fig. 7.In order to analyse the air distribution, this figure was obtained at t = 10 s, a point at which the tube had not yet reached a steady state at the air, as temperature of 240 °C. The temperature difference between the front and back of the tube decreases as the Z/D_{jet} ratio decreases. Therefore, the optimal Z/D_{jet} ratio is determined to be 2. Additionally, the reduced temperature difference in Tests 13 and 14 reflects an inversely proportional relationship between the Z/D_{jet} and Y/D_{jet} ratios.

3.1.5. Axial (X/D_{jet}) and circumferential (Y/D_{jet}) jets distribution

The X/D_{jet} and Y/D_{jet} ratios represent the number of jets in the system and their distribution, both of which have a high impact on heat transfer rates. Optimising these parameters is essential to enhance the thermal performance of the tube heater. Numerous studies have explored the effect of jet spacing on heat transfer rates in jet impingement systems. For instance, Singh et al. [22] investigated double jet impingement on a cylindrical target and examined X/D_{jet} ratios ranging from 4 to 20. They observed an increase in heat transfer rates as the X/D_{jet} value increased. Similarly, San and Chen [13] studied multiple jet impingement on a flat surface, focusing on X/D_{jet} ratios ranging from 2 to 8, and found that heat transfer rates increased with higher X/D_{jet} ratios. In their investigation on the heat transfer of a multiple air impingement jets on a flat target, Yong et al. [23] considered jet-to-jet spacing of between $2D_{jet}$ and $5D_{jet}$. They found as the decreasing jet-to-jet spacing increased the heat transfer rate, highlighting an optimum value of $3D_{jet}$. At lower values of $2D_{jet}$, air crossflow and jet interaction increased, reducing the heat transfer rate, and at higher values, the rate also decreased.

In this study, jet-to-jet spacing is analysed in terms of their axial distribution (X/D_{jet}) and circumferential distribution (Y/D_{jet}) to determine the optimal ratios for cylindrical impingement heating in the tube heater. This section cross-examines the two ratios, as presented in Table 6, which compares X/D_{jet} ratios ranging from 4 to 6 and Y/D_{jet} ratios ranging from 2 to 6 in Test 12 and Tests 15 to 31. The number of jets for each of these tests is provided in Table 7.

Table 8 and Table 9 provide data on the pressure drop and stagnation velocity for Test 12 and Tests 15 to 31. As it can be seen, as the number of jets decreases, both the pressure drop and stagnation velocity increase, in line with findings from previous studies [13,18,23].

Notable, it is impractical to consider the lowest X/D_{jet} and Y/D_{jet} values as this comes at the cost of high pressure drop (Table 8) and consequently high required fan power. Hence, Fig. 8 illustrates the heat transfer rate and the required fan power for varying X/D_{jet} and Y/D_{jet} ratios. It is evident that as X/D_{jet} and Y/D_{jet} ratios increase, both the heat transfer rate and fan power also increase. However, when Y/D_{jet} exceeds 4, the differences in heat transfer rates among different X/D_{jet} ratios become insignificant, whereas the differences in required fan power become more significant.

Table 6
Z/D_{jet} ratio analysis.

	Test 8	Test 11	Test 12	Test 13	Test 14
Z/D_{jet} Ratio	4	3	2	3	2
Inner shell diameter [mm]	106.9	86.9	66.9	86.9	66.9
Outer shell diameter [mm]	166.9	146.9	126.9	146.9	126.9
Y/D_{jet} Ratio	4	4	4	3.5	2.5
No. of Jets – Axially	5	5	5	5	5
No. of Jet – Circumferentially	8	7	5	8	8
Total Number of Jets	40	35	25	40	40
Total Jet inlet cross sectional area [mm^2]	3142	2749	2376	3142	3142
Pressure drop [Pa]	**14,087**	**17,997**	**33,081**	**14,214**	**15,063**
Stagnation velocity [m/s]	**191**	**220**	**291**	**192**	**192**
Heat transfer rate [W]	**1748**	**1963**	**2022**	**1843**	**1877**

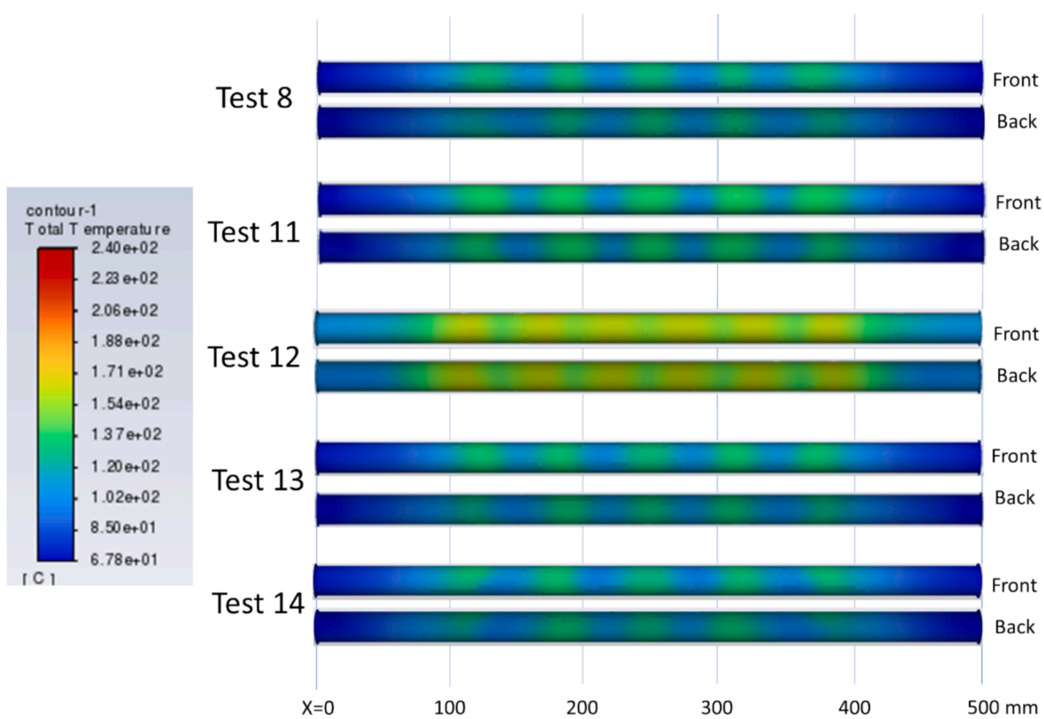

Fig. 7. Average tube temperature for varying Z/D_{jet} ratio – t = 10 s.

Table 7
X/D_{jet} and Y/D_{jet} ratio analysis.

		Y/D_{jet} 2	2.5	3	4	5	6
X/D_{jet}	4	Test 15	Test 16	Test 17	Test 18	Test 19	Test 20
	5	Test 21	Test 22	Test 23	Test 24	Test 25	Test 26
	6	Test 27	Test 28	Test 29	Test 12	Test 30	Test 31

Table 8
Number of nuzzles for X/D_{jet} and Y/D_{jet} ratio analysis.

		Y/D_{jet} 2	2.5	3	4	5	6
X/D_{jet}	4	88	64	56	40	32	24
	5	66	48	42	30	24	18
	6	55	40	35	25	20	15

Table 9
Pressure drop for varying X/D_{jet} and Y/D_{jet} ratios [Pa].

		Y/D_{jet} 2	2.5	3	4	5	6
X/D_{jet}	4	6119	8340	9628	14,236	21,420	36,117
	5	8287	11,196	14,099	24,105	36,299	61,451
	6	12,000	15,063	18,822	33,081	50,320	84,667

This observation highlights the advantage of utilising an X/D_{jet} ratio of 4 with Y/D_{jet} ratios of 4 and above (represented by Tests 18, 19, and 20). In these configurations, a lower fan power is required while still providing a uniform heat transfer rate to the tube (Fig. 9). Moreover, Test 18, with an X/D_{jet} ratio of 4 and a Y/D_{jet} ratio of 4, exhibits the most substantial difference between the required fan power and the provided heat transfer rate while operating at lower pressure drop and velocity (as indicated in Table 8 and Table 9).Therefore, based on these considerations, Test 18 with an X/D_{jet} ratio of 4 and a Y/D_{jet} ratio of 4 are selected as the optimum configuration for achieving a balance between fan power requirements and heat transfer performance.

3.1.6. *Jets diameter*

The jet diameter plays a crucial role in influencing the velocity profile of impinged air and its subsequent heat transfer rate to the steel tube. Optimising this parameter is essential to minimise material usage while maintaining the thermal performance of the system. Previous studies have investigated the impact of jet diameter, typically expressed as the ratio of jet diameter to the target diameter (D_{jet}/D_{target}) in jet impingement systems on cylindrical targets. These studies have showed contradictory results. Some studies, observed an increase in heat transfer coefficient with decreasing D_{jet}/D_{target}. These include Gua and Chung [36] who investigated the performance of the single jet in a semi-cylindrical target for D_{jet}/D_{target} ratio varying from 0.0218 to 0.125 for Reynolds numbers varying from 6,000 to 350,000. The authors observed the heat transfer coefficient to increase as the D_{jet}/D_{target} decreased. A similar conclusion was reached by Cornaro et al.[20] who experimentally investigated the heat transfer of impingement jets to convex semi-cylinder surfaces for D_{jet}/D_{target} ratio varying from 0.18 to 0.385 and Reynolds number of 6,000 to 16,000 as well as Lee [37] who investigated the local heat transfer on cylindrical targets for D_{jet}/D_{target} ratio varying from 0.1 to 0.5 and Reynolds number varying from 11,000 to 50,000.

In contrast, other studies reported a decrease in heat transfer rate with decreasing D_{jet}/D_{target}. These include Tawfek [21] who carried out experimental work to investigate the heat transfer distribution on a cylindrical target axially and circumferentially for D_{jet}/D_{target} ratio varying from 0.06 to 0.14 and Reynolds number varying from 3,800 to 40,000. The author found the heat transfer rate to decrease as D_{jet}/D_{target} decreased. A similar conclusion was reached by Singh et al. [18] who carried out experimental and numerical analysis on single air jet impingement for D_{jet}/D_{target} ratio varying from 0.11 to 0.25 and Reynolds number varying from 10,000 to 25,000, as well as Csenyei and Straatman [19] carried out a numerical investigation on multiple jet impingement cooling on a cylindrical target in a cement kiln for D_{jet}/D_{target} ratios varying from 0.15 to 0.31.

To address this inconsistency, Wang et al. [28] conducted experiments and concluded that the relationship between D_{jet}/D_{target} and heat transfer rate depends on the position relative to the potential core of the jet: Below the potential core, the heat transfer rate decreases as the D_{jet}/D_{target} ratio increases, in line with results of Gau and Chung [36], Cornaro et al. [20] and Lee [37]. Above the potential core, the heat transfer rate increases as the D_{jet}/D_{target} ratio increases, in line with results of Tawfek [21], Singh et al. [18] and Csenyei and Straatman [19].

Therefore, when analysing different jet diameters for the tube heater, it is essential to consider whether the airflow exceeds the potential core. The primary jet diameter used in this study was 10 mm, corresponding to a D_{jet}/D_{target} ratio of 0.372. To assess its impact on heat transfer in the tube heater, Test 17 is compared to Tests 32, 33, and 34, which have D_{jet}/D_{target} ratios ranging from 0.409 to 0.483, as presented in Table 10. Increasing the D_{jet}/D_{target} value results in a larger total inlet cross-sectional area for the jets while reducing the number of jets.

The results of the jet diameter analysis in Tests 18, 32, 33, and 34, presented in Table 10, indicate that the pressure drop, stagnation velocity, and heat transfer rate increase with the D_{jet}/D_{target} ratio. On one

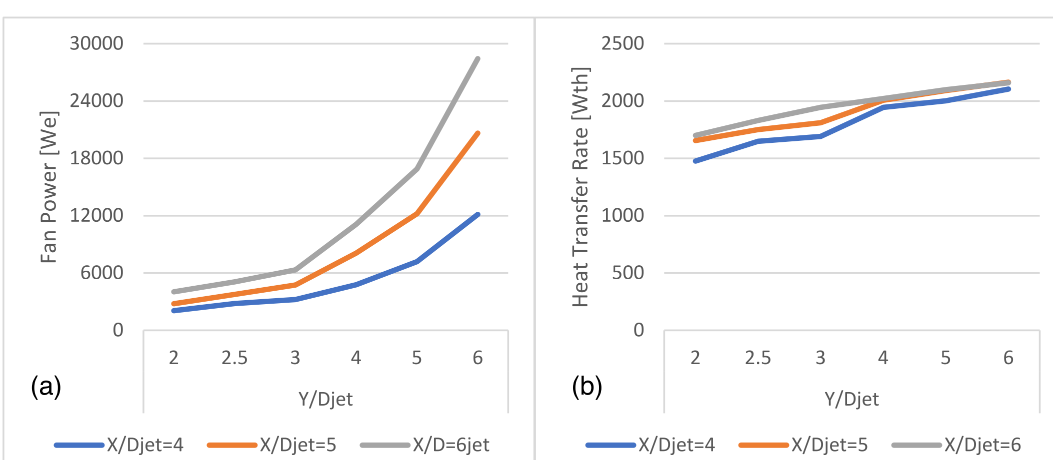

Fig. 8. Required fan power (a) and heat transfer rate (b) for varying X/D_{jet} and Y/D_{jet} ratios.

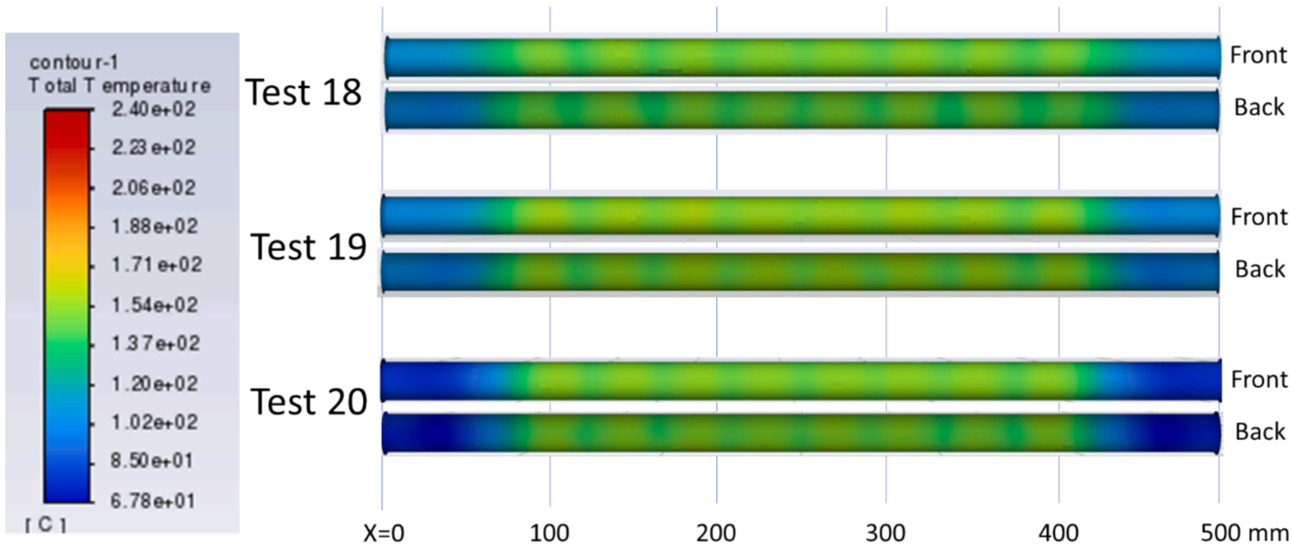

Fig. 9. Tube temperature contour for varying X/D_{jet} and Y/D_{jet} ratios at t = 10 s.

Table 10
Stagnation velocity for varying X/D_{jet} and Y/D_{jet} ratios [m/s].

		Y/D_{jet} 2	2.5	3	4	5	6
X/D_{jet}	4	95	124	143	194	234	297
	5	129	160	180	241	308	401
	6	170	192	217	291	267	420

hand, this suggests that the potential core has not been reduced in these cases, as defined by Wang et al. [28], observing a similar behaviour to that observed by Gau and Chung [36], Cornaro et al. [20] and Lee [37]. On the other hand, it also reflects the directly proportional effect of the number of jets in the system with varying D_{jet}/D_{target} ratio on the thermal performance, complementing the conclusion of Rao et al. [10].

Moreover, Test 32 exhibited a slightly lower heat transfer rate compared to Test 18 but with a more substantial reduction in pressure drop, which will result in lower required fan power, as shown in Fig. 10. Therefore, based on the results, the optimum jet diameter (D_{jet}) for the tube heater is determined to be 11 mm, corresponding to a D_{jet}/D_{target} ratio of 0.409.

The results of the parametric analysis have been summarised in Table 11, which presents the optimum design of the tube heater. The tube heater with the presented optimum design was manufactured and assessed experimentally (Section 2.2) to validate the numerical model

Table 11
Jet diameter analysis.

	Test 18	Test 32	Test 33	Test 34
Jet Diameter [mm]	10	11	12	13
D_{jet}/D_{target}	0.372	0.409	0.446	0.483
Inner shell diameter [mm]	66.9	70.9	74.9	78.9
Outer shell diameter [mm]	126.9	130.9	134.9	138.9
No. of Jets – axially	8	7	7	6
No. of Jet – Circumferential	5	5	5	5
Total Number of Jets	40	35	35	30
Total Jet inlet cross-sectional area [mm^2]	3142	3326	3958	3982
Pressure drop [Pa]	**15,179**	**13,701**	**13,475**	**10,162**
Stagnation velocity [m/s]	**194**	**185**	**162**	**159**
Heat transfer rate [W]	**1926**	**1925**	**1890**	**1741**

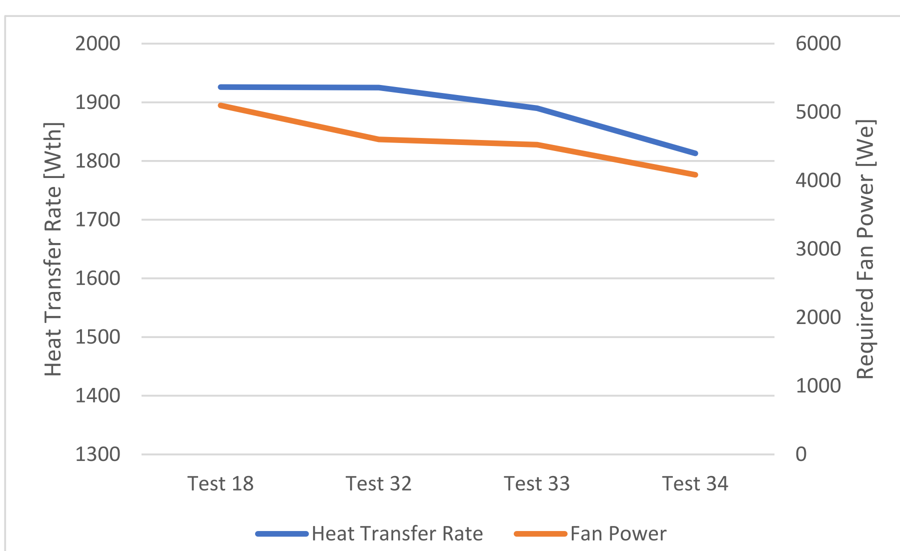

Fig. 10. Heat Transfer rate and required fan power for varying D_{jet}/D_{tube} ratios.

carried out in this section.

3.2. Experimental results

The experimental results for the tube heater with a steady tube are depicted in Fig. 11. These experimental findings closely align with the numerical results, as demonstrated by a high R-squared value of 0.989. There are notable distinctions to observe between the two models. Initially, the experimental model records a higher temperature, which can be attributed to radiative heat transfer effects, a factor not considered in the numerical model. Subsequently, after stabilisation, the experimental model registers a lower temperature due to thermal losses inherent in the experimental setup, which were not accounted for in the numerical model. Consequently, the experimental model stabilises at 144 °C, while the numerical model stabilises at 149.5 °C, resulting in a 3 % difference. In a similar study by Tawfek [19], comparing experimental and theoretical outcomes of a single jet impinging on a cylindrical target, an average difference of 4.5 % was noted. This level of error was deemed acceptable, falling within the defined range of below 10 % [21]. Therefore, the 3 % difference obtained in this case is also considered acceptable. These results validate the numerical model and provide valuable insights into the tube heater's thermal behaviour under steady conditions.

Fig. 12 provides a comparison between the numerical and experimental results for the steady tube test. It is evident that all the numerical results fall within a 10 % error margin of the experimental results, confirming the validity of the numerical models presented in Section 3.1. This close agreement between the experimental and numerical findings further supports the accuracy of the developed models. Compared to other studies that validated their numerical results experimentally following a similar method, such as Chi et al. [35], Penumadu and Rao [10] and Singh et al. [22], who deduced the numerical results to be within 20 %, 10 % and 4.5 %, respectively, of the experimental results, reveals that the results obtained for this study (Fig. 12) are within a predicted range.

Table 12 presents the uncertainty of the experimental results due to error factors in the equipment used, the pitot tube and the thermocouples. It can be seen that the pitot tube has an uncertainty of ± 1.5 % (±0.167 m/s) whereas the thermocouples 1.67 %-2.11 % (±2.5 °C). These values are well within the acceptable range of below 10 %, as defined by Taylor [32] indicating that the potential errors associated with velocity and temperature measurements are reasonably low and do not significantly affect the accuracy of the experimental results. Comparing to other studies who experimentally evaluated impingement systems such as Wang et al. [28], Singh et al. [18,22] and Baydar and Ozmen [31], who deduced an insignificant uncertainty of 4,7%, 8.2 % and 1–6 %, respectively, reveals that the uncertainties in this study are less significant (Table 13).

4. Conclusion & recommendations

In conclusion, this paper presented numerical and experimental models of a novel tube heater designed to integrate innovative solar thermal system to the powder-based coating process. The parametric analysis conducted in this study have provided valuable insights into the effect of critical parameters on the thermal performance of multiple air jets impingement systems with cylindrical target similar to the tube heater. Results showed the following:

- The tube heater's length, funnel height and jets' height showed to minimally affect the thermal performance and provide material savings; hence, minimal values of 500 mm, 50 mm and 5 mm were selected, respectively.
- The Z/D_{jet} and D_{jet} that showed an inversely proportional effect on the thermal performance with optimum values of 2 and 11 mm, respectively
- The X/D_{jet} and Y/D_{jet} that showed a balance between the heat transfer rate and the required fan power at a ratio of 4 for both.
- The experimental work robustly validated the numerical models with R-squared value of 0.992, confirming their accuracy and reliability.

Numerical limitations include those of the SST k-w which, although was found to best predict air flow and heat transfer in multiple jet impingement systems, may overpredict turbulence levels in high irradiance regions. Experimental limitations included limited fan power and valves' temperature tolerance that prevented validation at temperatures higher than 150 °C, as well as limited manufacturing and financial limitations that prevented investigating more critical parameters such as the jets shape and its inclinations angle.

Looking ahead, several aspects for future research and exploration are recommended. Firstly, enhancing the experimental setup to evaluate the dynamic numerical model of the novel tube heater, as presented in Tannous et al. [38], would provide a more comprehensive understanding of its transient behaviour. Secondly, upgrading the fan and valves in the air loop will allow the test rig to test the performance of the tube

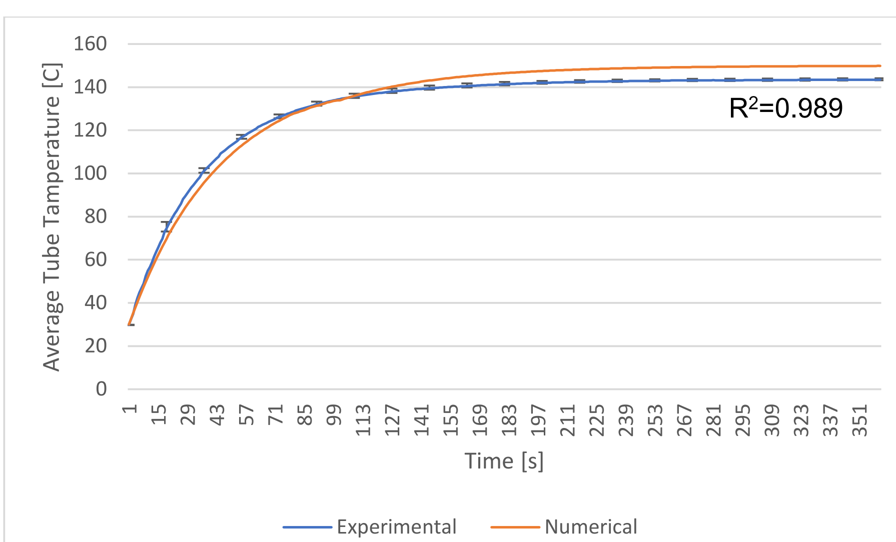

Fig. 11. Average tube temperature achieved in the experimental and numerical models with a steady tube.

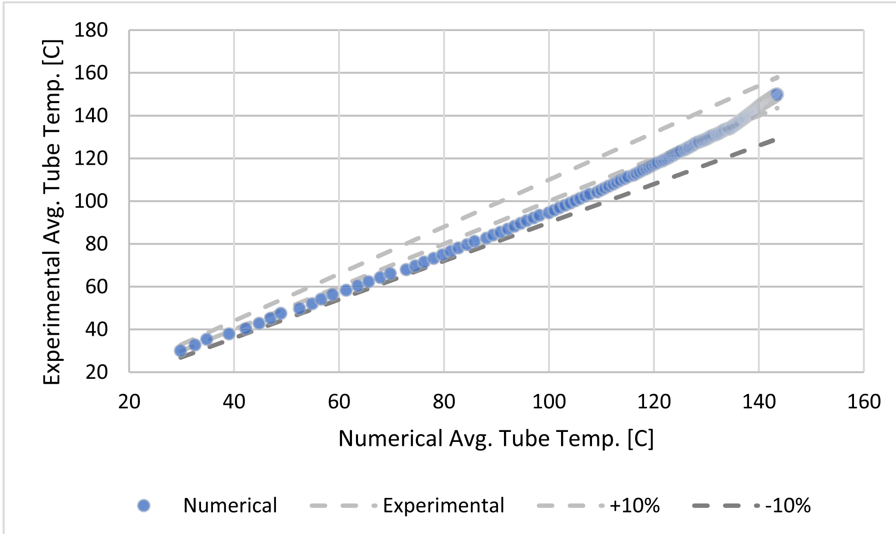

Fig. 12. Comparison between the experimental and numerical results.

Table 12
Optimum design of the tube heater.

Parameter		Value
Tube heater length	Inner shell length [mm]	500
	Outer shell length [mm]	300
	Steel tube length [mm]	500
Jet length [mm]		5
Funnel height [mm]		50
Z/D_{jet} Ratio		2
Y/D_{jet} Ratio		4
X/D_{jet} Ratio		4
Jet diameter [mm]		11

Table 13
Uncertainty analysis.

	Pitot Tube	Thermocouples
Uncertainty	±0.167 m/s ±1.5 %	±2.5 °C ±1.67 %-2.11 %

heater at a higher air flow rate and temperature. Evaluating heat losses in the test rig and taking suitable measures to reduce them can further help increase its operation temperature. Thirdly, investigating the effect of jet shape on heat transfer rate when impinging on cylindrical targets could yield valuable insights into further performance optimisation. Fourthly, examining the tube heater's performance under different tube velocities is essential to assess its adaptability to various operational conditions. Fifthly, evaluating the impact of different inlet diameters on heat transfer performance can lead to improved system efficiency. Sixthly, exploring more efficient methods for attaching thermocouples to the steel tube can enhance measurement accuracy and repeatability. Lastly, developing a theoretical model of the tube heater for comparison with numerical and experimental models would contribute to a deeper theoretical understanding of its behaviour. These future endeavours will advance the field of tube heater technology and its applications in sustainable energy systems.

CRediT authorship contribution statement

Hadi Tannous - performed experimental work and write the article, **Valentina Stojceska** - revised and edited, **Jose Tavares** - contributed to the experimental work, **Savvas Tassou** - supervised the work.

Declaration of competing interest

The authors declare that they have no known competing financial interests or personal relationships that could have appeared to influence the work reported in this paper.

Acknowledgments

This project is funded from the European Union (EU) Horizon 2020 research and innovation programme, Application of Solar Energy in Industrial processes (ASTEP), under grant agreement No 884411.

Data availability

Data will be made available on request.

References

[1] L. Kumar, M. Hasanuzzaman, N.A. Rahim, Global advancement of solar thermal energy technologies for industrial process heat and its future prospects: a review, Energy Convers Manag 195 (2019) 885–908, https://doi.org/10.1016/j.enconman.2019.05.081.
[2] European Commission. Climate Strategies and Targets, 2007.
[3] H. Tannous, V. Stojceska, S. Tassou, The Use of Solar Thermal Heating in SPIRE and Non-SPIRE Industrial Processes, Sustainability 15 (2023) 7807, https://doi.org/10.3390/su15107807.
[4] Muster-Slawitsch B, Meitz S, Frank E. Solar Heat Integrations in Industrial Processes. 2020.
[5] AEE INTEC. Solar Thermal Plants Database 2020. http://ship-plants.info/ (accessed August 7, 2020).
[6] European Commission. Energy Balance Sheet – 2015 edition. 2017.
[7] H.M. Tahar, M.T. Hannachi, B. Dahache, E. Guelloudje, Effect of heating of steel tubes by induction at high frequency, Microwave Review 24 (2018) 23–27.
[8] M. Barnetche, L.F. González-Portillo, R. Abbas, Optimum integration of latent heat storage in a solar thermal system for industrial processes: In series or in parallel? Appl. Therm. Eng. 232 (2023) https://doi.org/10.1016/j.applthermaleng.2023.121090.
[9] R. Abbas, R. Barbero, A. Rovira, M. Barnetche, Sun Dial, a new collector for solar heat for industrial processes: optical and thermal design, Therm. Sci. Eng. Progr. 44 (2023), https://doi.org/10.1016/j.tsep.2023.102025.
[10] P.S. Penumadu, A.G. Rao, Numerical investigations of heat transfer and pressure drop characteristics in multiple jet impingement system, Appl. Therm. Eng. 110 (2017) 1511–1524, https://doi.org/10.1016/j.applthermaleng.2016.09.057.
[11] NK, Chougule, G v. Parishwad, P.R. Gore, S. Pagins, S.N. Sapali, CFD Analysis of Multi-jet Air Impingement on Flat Plate. Proceedings of the World Congress on Engineering, 2011.
[12] A. Dewan, R. Dutta, B. Srinivasan, Recent trends in computation of turbulent jet impingement heat transfer, Heat Transfer Eng. 33 (2012) 447–460, https://doi.org/10.1080/01457632.2012.614154.

[13] J.Y. San, J.J. Chen, Effects of jet-to-jet spacing and jet height on heat transfer characteristics of an impinging jet array, Int. J. Heat Mass Transf. 71 (2014) 8–17, https://doi.org/10.1016/j.ijheatmasstransfer.2013.11.079.

[14] F. Afroz, M.A.R. Sharif, Numerical study of turbulent annular impinging jet flow and heat transfer from a flat surface, Appl. Therm. Eng. 138 (2018) 154–172, https://doi.org/10.1016/j.applthermaleng.2018.04.007.

[15] F.B. Baz, E.A. Elshenawy, S.A. El-Agouz, Y.A.F. El-Samadony, S.A. Marzouk, Experimental study on air impinging jet for effective cooling of multiple protruding heat sources, Int. J. Therm. Sci. 196 (2024), https://doi.org/10.1016/j.ijthermalsci.2023.108707.

[16] A. Sharma, S. Thakur, P. Dhiman, R. Kumar, Effect of jet-impingement and surface roughness on performance of solar air heater: Experimental study and its optimization, Expert Syst. Appl. 238 (2024), https://doi.org/10.1016/j.eswa.2023.122208.

[17] Rao AG, Yeshayahou L, Kitron-Belinkov M. Heat transfer characteristics of a multiple jet impingement system Novel Propulsion System Architectures View project Sustainable Aviation View project. 2009.

[18] D. Singh, B. Premachandran, S. Kohli, Effect of nozzle shape on jet impingement heat transfer from a circular cylinder, Int. J. Therm. Sci. 96 (2015) 45–69, https://doi.org/10.1016/j.ijthermalsci.2015.04.011.

[19] C. Csernyei, A.G. Straatman, Forced convective heat transfer on a horizontal circular cylinder due to multiple impinging circular jets, Appl. Therm. Eng. 105 (2016) 290–303, https://doi.org/10.1016/j.applthermaleng.2016.05.166.

[20] Cornaro C, Fleischer AS, Rounds M, Goldstein RJ. Jet impingement cooling of a convex semi-cylindrical surface. vol. 40. 2001.

[21] Tawfek AA. Heat transfer due to a round jet impinging normal to a circular cylinder. 1999.

[22] D. Singh, B. Premachandran, S. Kohli, Double circular air jet impingement cooling of a heated circular cylinder, Int. J. Heat Mass Transf. 109 (2017) 619–646, https://doi.org/10.1016/j.ijheatmasstransfer.2017.02.035.

[23] S. Yong, J.Z. Zhang, G.N. Xie, Convective heat transfer for multiple rows of impinging air jets with small jet-to-jet spacing in a semi-confined channel, Int. J. Heat Mass Transf. 86 (2015) 832–842, https://doi.org/10.1016/j.ijheatmasstransfer.2015.03.073.

[24] C.N. Jordan, L.M. Wright, D.C. Crites, Impingement heat transfer on a cylindrical, concave surface with varying jet geometries, J. Heat Transfer 138 (2016), https://doi.org/10.1115/1.4034180.

[25] L. Shi, X. Zhu, Z. Du, Study on convective heat transfer characteristics of inclined jet impinging cylindrical target surface in the confined space, Appl. Therm. Eng. 218 (2023), https://doi.org/10.1016/j.applthermaleng.2022.119316.

[26] Hassan Mroue. NUMERICAL AND EXPERIMENTAL INVESTIGATION OF A MULTI-PASS HEATPIPE-BASED HEAT EXCHANGER. Brunel University London, 2018.

[27] ANSYS Inc. ANSYS FLUENT 12.0 User's Guide 2009.

[28] Y.Q. Zu, Y.Y. Yan, J.D. Maltson, CFD Prediction for Multi-Jet Impingement Heating, ASME Turbo Expo (2009).

[29] Menter F, Menter FR, Kuntz M, Langtry R. Ten years of industrial experience with the SST turbulence model. n.d.

[30] ASTEP. ASTEP's BRUL & AMPT Meeting 2021.

[31] E. Baydar, Y. Ozmen, An experimental and numerical investigation on a confined impinging air jet at high Reynolds numbers, Appl. Therm. Eng. 25 (2005) 409–421, https://doi.org/10.1016/j.applthermaleng.2004.05.016.

[32] J. Tylor, An introduction to error analysis: The study of uncertainties in physical measurements, 2nd ed., California, USA, 1997.

[33] H. Mroue, J.B. Ramos, L.C. Wrobel, H. Jouhara, Experimental and numerical investigation of an air-to-water heat pipe-based heat exchanger, Appl. Therm. Eng. 78 (2015) 339–350, https://doi.org/10.1016/j.applthermaleng.2015.01.005.

[34] TC Direct. Technical Data of Type K Thermocouples 2023.

[35] Z. Chi, R. Kan, J. Ren, H. Jiang, Experimental and numerical study of the anti-crossflows impingement cooling structure, Int. J. Heat Mass Transf. 64 (2013) 567–580, https://doi.org/10.1016/j.ijheatmasstransfer.2013.04.052.

[36] C. Gau, C.M. Chung, Surface curvature effect on slot- air-jet impingement cooling flow and heat transfer process, J. Heat Transfer 113 (1991) 858–864, https://doi.org/10.1115/1.2911214.

[37] Lee DH, Chung YS, Kim DS. Turbulent flow and heat transfer measurements on a curved surface with a fully developed round impinging jet. 1997.

[38] Tannous H, Stojceska V, Tassou S. Numerical Analysis of a Solar-Powered Tube Heater. Proceedings of the 9th World Congress on Mechanical, Chemical, and Material Engineering, Avestia Publishing; 2023. https://doi.org/10.11159/htff23.224.